Supporting information:

Effect of ferroelectric polarization on oxygen evolution reaction: a theoretical study of MIrSn$_2$S$_6$ (M = Bi, Mn, and Sb)

Haoyun Bai[1], Weng Fai Ip[2], Wenlin Feng[3], and Hui Pan[1,2]*

[1] Institute of Applied Physics and Materials Engineering, University of Macau, Macao SAR, 999078, P.R. China

[2] Department of Physics and Chemistry, Faculty of Science and Technology, University of Macau, Macao SAR, 999078, P. R. China

[3] School of Science, Chongqing University of Technology, Chongqing, 400054, P. R. China

*Corresponding Author

H. Pan: huipan@um.edu.mo (email), +853 88224427 (tel.), +853-88222454 (fax)

Supporting Notes

1. Derivation of free energy-potential relationship and surface capacitance

The potential-dependent free electrochemical energy of the electrode/electrolyte interface can be calculated as[1-3]

$$E_{free}(q) = E_{SCF}(q) + E_{corr}(q) - q\phi_q(f)$$

In the formula, E_{SCF} is the self-consistent energy obtained by DFT calculations depending on unbalanced electron number q of the system, E_{corr} is the correction to the E_{SCF} due to the homogeneous background charge, which is obtained by using the average electrostatic potential of the supercell $\langle \overline{V}_{tot} \rangle$:

$$E_{corr} = \int_0^q \langle \overline{V}_{tot} \rangle dQ$$

$-q\phi_q(f)$ is the work function of the slab. The potential vs. SHE of the charged slab is defined as

$$U_q(V/SHE) = -4.6 - \phi_q(f)/eV$$

The free energy is a continuous function of potential and related to the capacitance of the surface. The quadratic form is consistent with a capacitor created by the charged-slab/background-charge system:

$$E_{free}(U) = -\frac{1}{2}C(U - U_0)^2 + E_0$$

where U_0 refers to the potential of zero charge (PZC), E_0 is the energy in zero-potential, and C is the capacitance of the surface.

In the calculation, we change the number of charges from $-2.0e$ to $+2.0e$ with increments of 1e based on the balanced charge. The capacitance C can be obtained by fitting the free energy in five potential values. However, we found that when add 2e in the system, the electronic property of the system is greatly affected, and the obtained free energy is obviously shifted from the quadratic curve compared with other points (see the leftmost point in each curve in Figure 5 & S20). Thus, only four points are used to obtain the quadratic $E_{free} \sim U$ relationship, resulting in a good quadratic relationship as the coefficient of determination (R^2) of fitting exceeds 0.99.

Supporting Tables

Table S1. The lattice constant (a), thickness (t), total energy (E_0), formation energy per lattice (E_f), the energy difference (ΔE) between energy with (E_M) and without (E_{NM}) spin polarization ($\Delta E = E_M - E_{NM}$), and total magnetic moment (magmom) per lattice of MIrSn$_2$S$_6$ (M = Bi, Mn, Sb, and In).

	state	a (Å)	t (Å)	E_0 (eV)	E_f (eV)	ΔE (meV)	magmom (μ_B)
Bi	FE	6.549	4.461	−48.006	−2.889	0.000	0.000
	PE	6.566	4.722	−47.010	−1.893	0.000	0.000
Mn	FE	6.239	3.941	−53.892	−4.344	−679.449	2.000
	PE	6.208	4.419	−53.374	−3.826	−602.209	2.080
Sb	FE	6.476	4.476	−48.120	−2.766	0.000	0.000
	PE	6.401	4.915	−47.909	−2.555	0.000	0.000
In	FE	6.436	4.310	−47.747	−3.958	0.000	0.000
	PE	6.530	3.915	−46.289	−2.500	0.000	0.000

Table S2. The total energy of PE, FE, and AFE states and energy difference between FE and AFE states of $MIrSn_2S_6$ (M = Bi, Mn, Sb, and In) in a 2×2 supercell. Unit: eV.

	Bi	Mn	Sb	In
E_{PE}	−188.039	−213.465	−191.635	−185.138
E_{FE}	−192.022	−215.571	−192.482	−190.989
E_{AFE}	−192.137	−216.018	−192.390	−191.302
$E_{FE}−E_{AFE}$	0.115	0.447	−0.091	0.313
$E_{FE}−E_{PE}$	−3.983	−2.106	−0.847	−5.851

Table S3. The elastic constants of FE-$MIrSn_2S_6$ (M = Bi, Mn, Sb, and In). Unit: GPa.

	C_{11}	C_{12}	C_{66}
Bi	25.321	8.680	8.320
Mn	30.227	8.588	10.819
Sb	24.139	6.912	8.513
In	30.298	8.260	11.019

Table S4. The total energy of ferromagnetic (E_{FM}), anti-ferromagnetic (E_{AFM}), and non-magnetic (E_{NM}) states, and exchange energy ($E_{ex} = E_{FM} − E_{AFM}$) of PE-, FE-, and AFE-$MnIrSn_2S_6$ calculated in 2×2×1 supercell. Unit: eV.

	E_{FM}	E_{AFM}	E_{NM}	E_{ex}
PE	−213.465	−213.185	−211.074	−0.280
FE	−215.571	−215.022	−212.857	−0.549
AFE	−216.018	−215.562	−212.805	−0.456

Table S5. Summary of the representative OER performance by DFT calculation in literatures.

Electrocatalyst	Overpotential (V)	Ref
β-CoOOH	0.55	[4]
$Ir_{0.75}Ni_{0.25}O_2$	~ 0.5	[5]
$Ni_6(SCH_3)_{12}O_5$	0.45	[6]
N-graphene	0.405	[7]
Mo-WO_3	0.61	[8]
Ir/pyrrolic-N_4-G	0.32	[9]
S doped C_3N_4	0.77	[10]
MoS_2/g-C_3N_4	0.78	[11]
W-SnO_2	1.12	[12]

CoOOH	0.50	13
γ-(Fe,Ni)OOH	0.42	14
β-CoOOH (001)	0.85	15
Co-TaS$_2$	0.93	16
Cr$_4$B$_6$O$_6$	0.56	17
PE-SbIrSn$_2$S$_6$	0.54	This work

Supplementary Figures
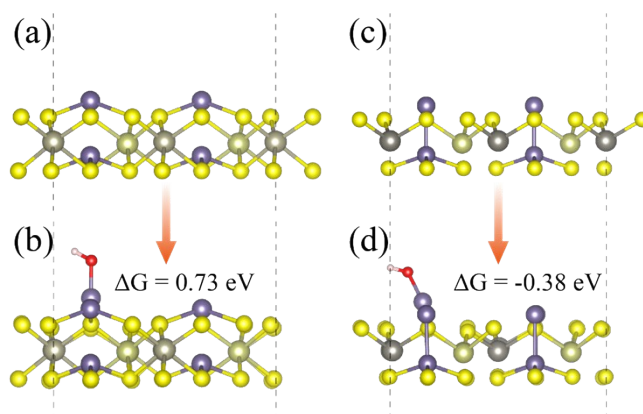
Figure S1. The structure of ReIrGe$_2$S$_6$ (a) before and (b) after adsorbing *OH. The structure of WIrGe$_2$S$_6$ (c) before and (d) after adsorbing *OH. The adsorption energies are marked in the figure.
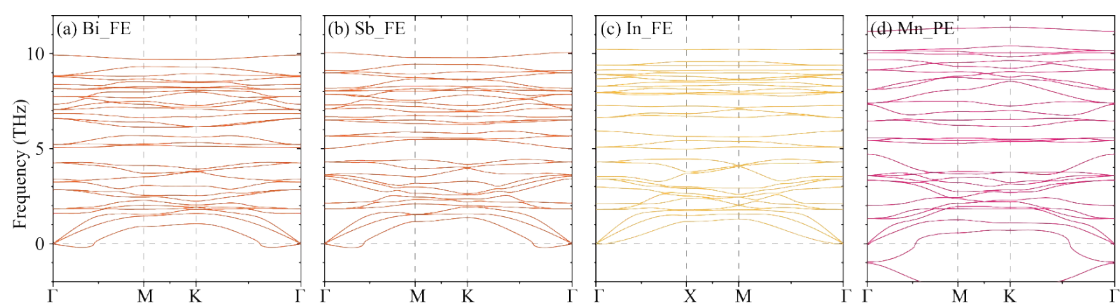

Figure S2. The calculated phonon dispersions of (a) FE-BiIrSn$_2$S$_6$, (b) FE-SbIrSn$_2$S$_6$, (c) FE-InIrSn$_2$S$_6$, and (c) PE-MnIrSn$_2$S$_6$.
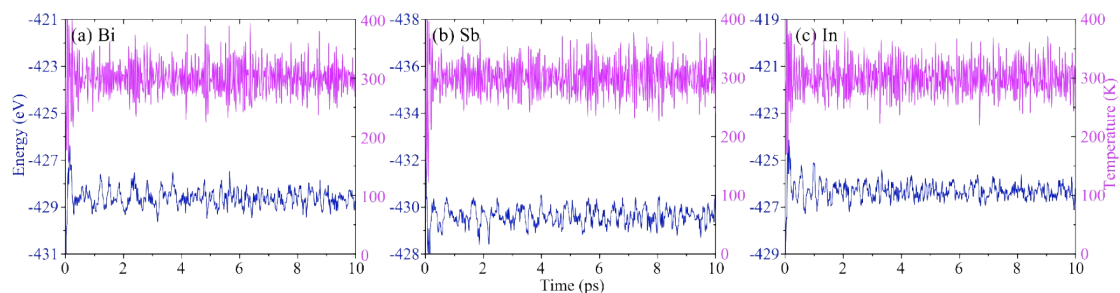
Figure S3. The *ab initio* molecular dynamics (AIMD) simulations for (a) FE-BiIrSn$_2$S$_6$, (b) FE-SbIrSn$_2$S$_6$, and (c) FE-InIrSn$_2$S$_6$.
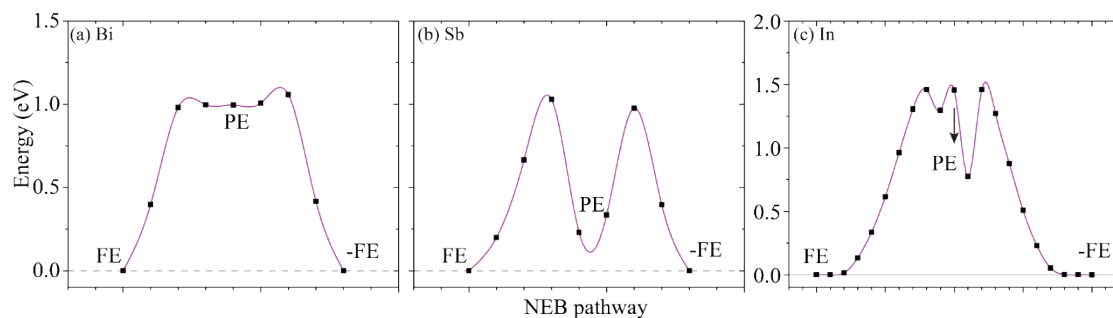
Figure S4. The minimum energy pathway in the polarization reverse process for (a) BiIrSn$_2$S$_6$, (b) SbIrSn$_2$S$_6$, and (c) InIrSn$_2$S$_6$.
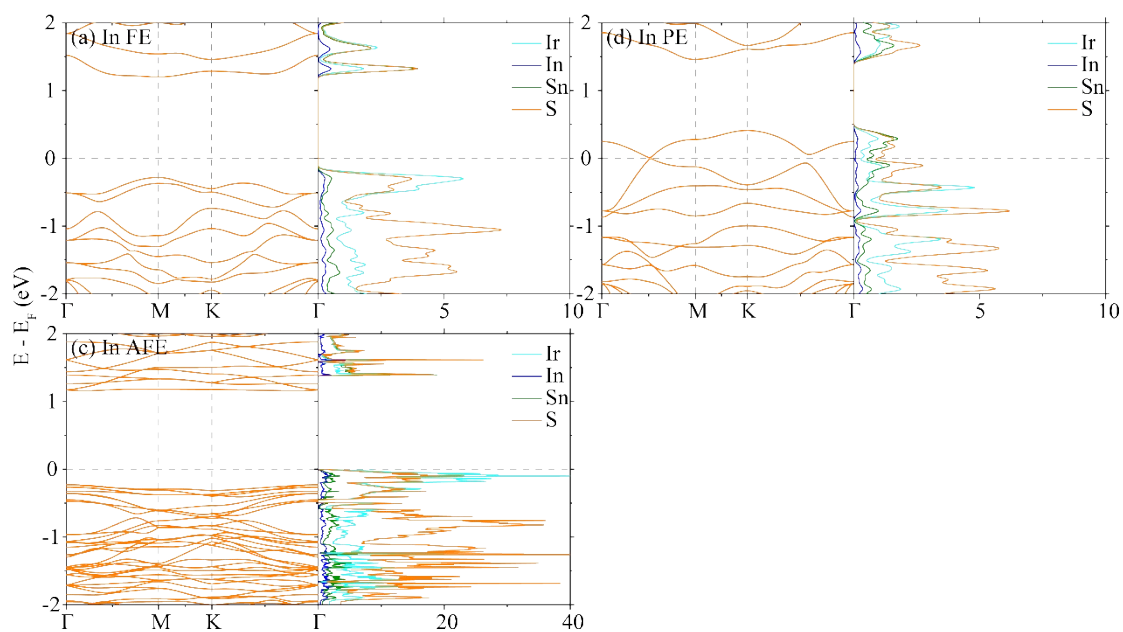
Figure S5. The band and DOS of (a) FE-, (b) PE-, and (c) AFE-InIrSn$_2$S$_6$.
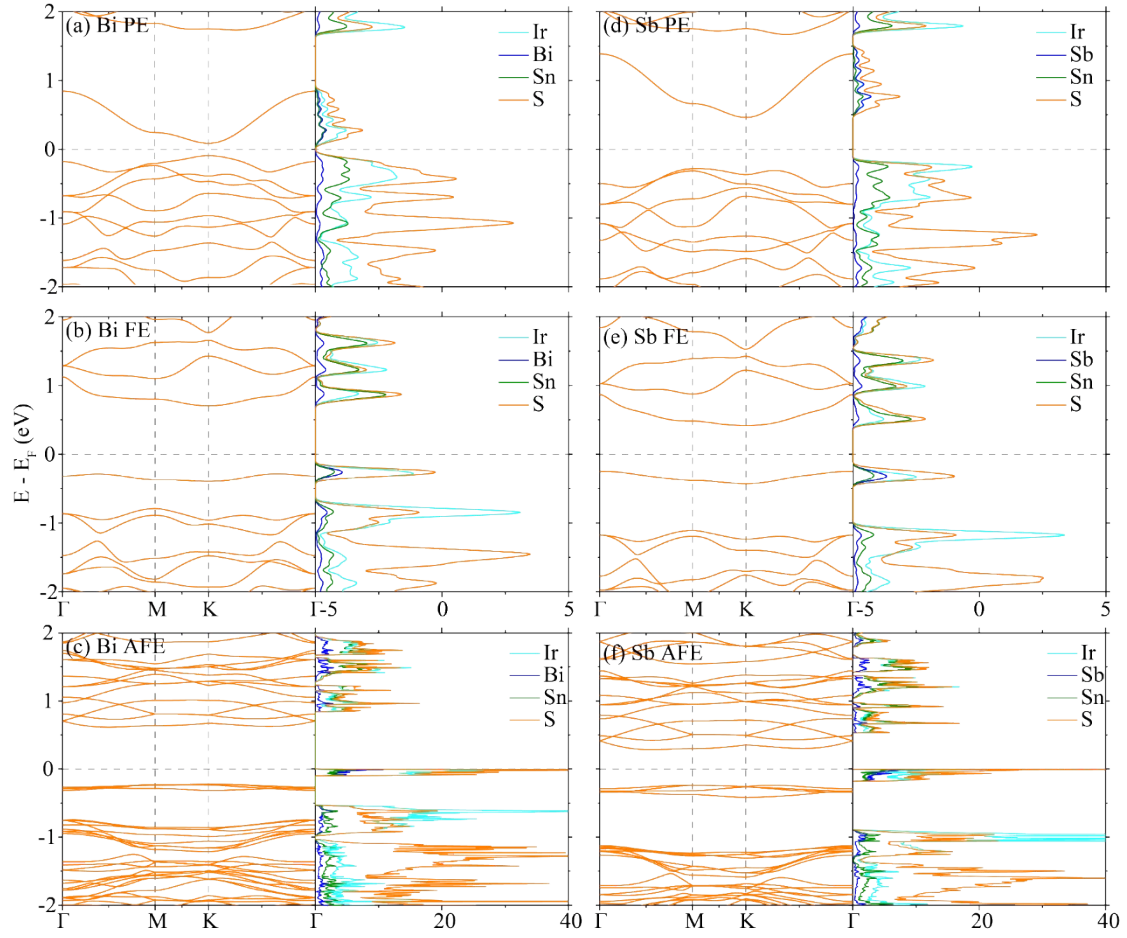
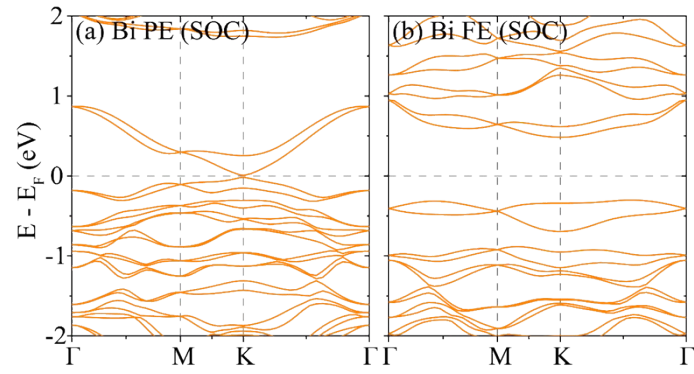Figure S6. The band and DOS of (a) PE-, (b) FE-, and (c) AFE-BiIrSn$_2$S$_6$, (d) PE-, (e) FE-, and (f) AFE-SbIrSn$_2$S$_6$.

Figure S7. The band structures of (a) PE- and (b) FE-BiIrSn2S6 with spin-orbital coupling.
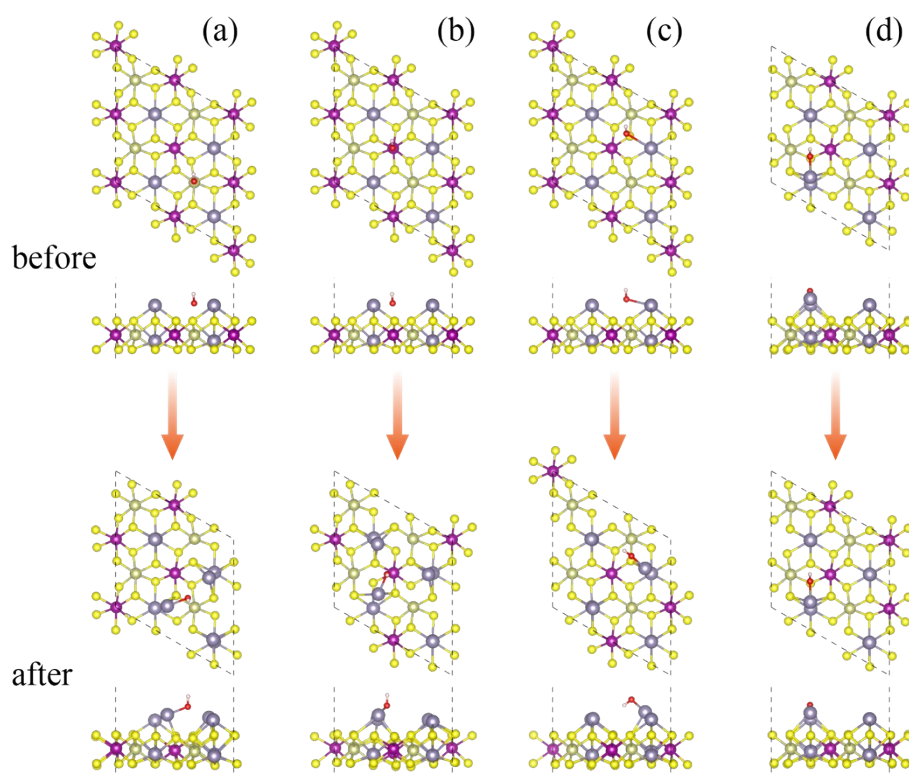
Figure S8. The possible active sites on FE-MIrSn$_2$S$_6$. All initial adsorption configurations are optimized into the similar configuration finally.
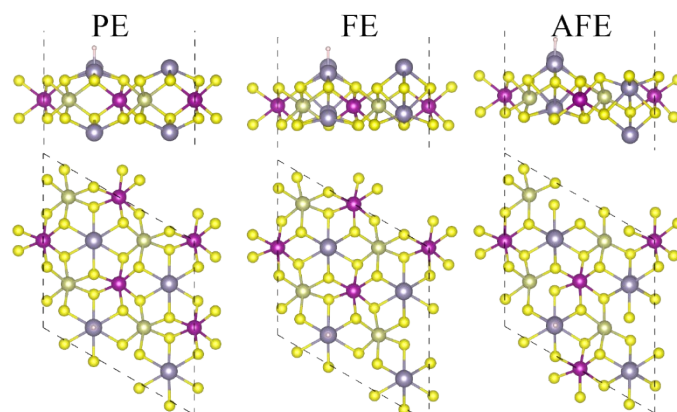

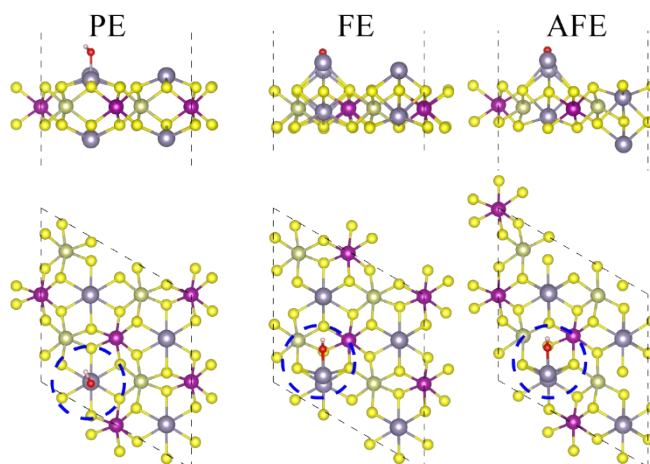Figure S9. Adsorption configuration of *H on PE-, FE-, and AFE-MnIrSn$_2$S$_6$ surface.

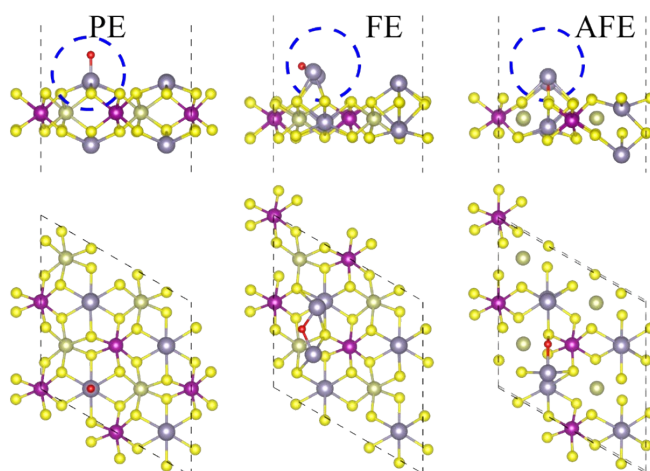Figure S10. Adsorption configuration of *OH on PE-, FE-, and AFE-MnIrSn$_2$S$_6$ surface.

Figure S11. Adsorption configuration of *O on PE-, FE-, and AFE-MnIrSn$_2$S$_6$ surface.
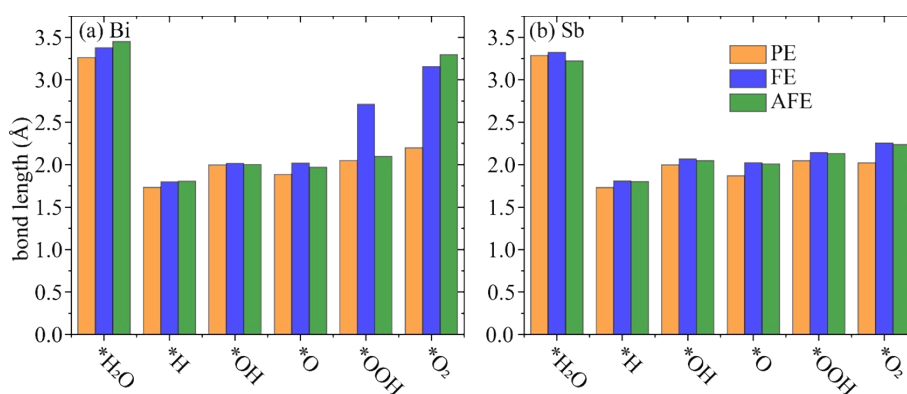

Figure S12. The comparation of bond length between Sn and intermediate on PE-, FE-, and AFE- (a) BiIrSn$_2$S$_6$ and (b) SbIrSn$_2$S$_6$ surface.
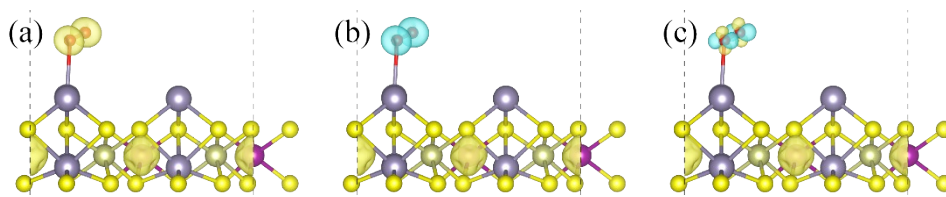
Figure S13. The different spin states of *OO on FE-MnIrSn$_2$S$_6$: magmom = (a) 10 μ_B, (b), 6.5 μ_B and (c) 8 μ_B. The yellow (clan) indicates spin up (down). The isosurface is 0.02e/Å^3.
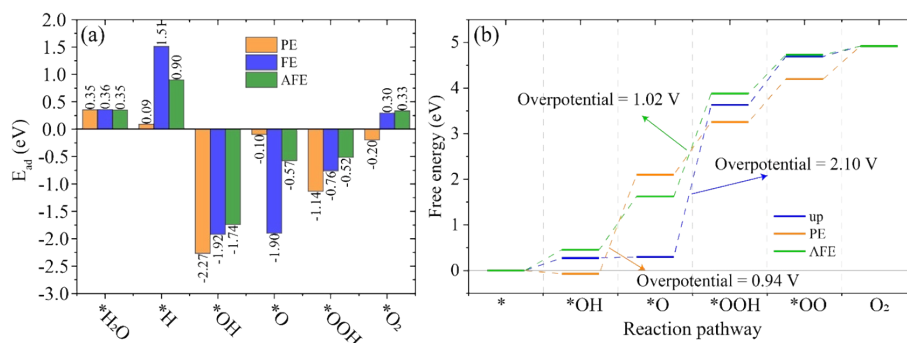

Figure S14. The (a) adsorption energy of intermediates and (b) diagrams of Gibbs free energy change in the OER process on PE-, FE-, and AFE-BiIrSn$_2$S$_6$ surface. The overpotential is marked in the figure.
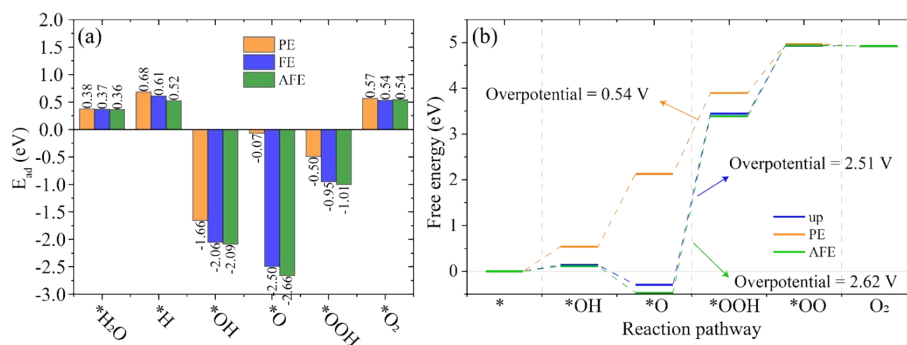

Figure S15. The (a) adsorption energy of intermediates and (b) diagrams of Gibbs free energy change in the OER process on PE-, FE-, and AFE-SbIrSn$_2$S$_6$ surface. The overpotential is marked in the figure.
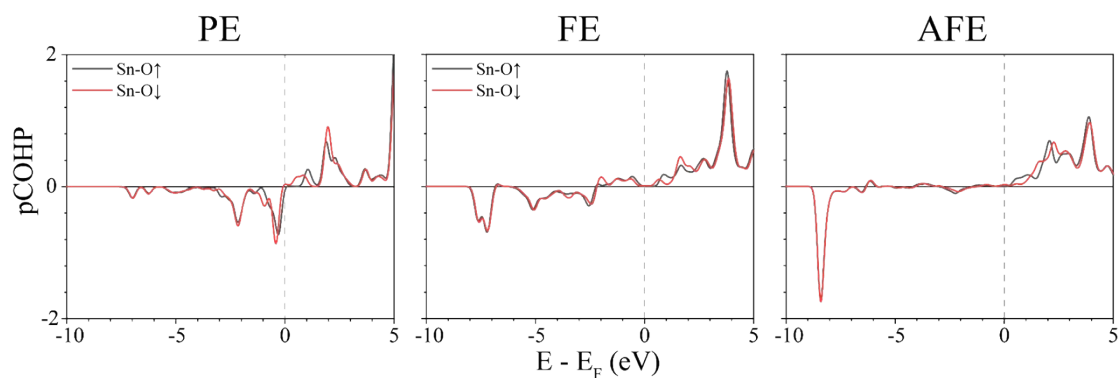
Figure S16. The COHP of Sn-O bonding in *O intermediate on PE-, FE-, and AFE-MnIrSn$_2$S$_6$ surface.
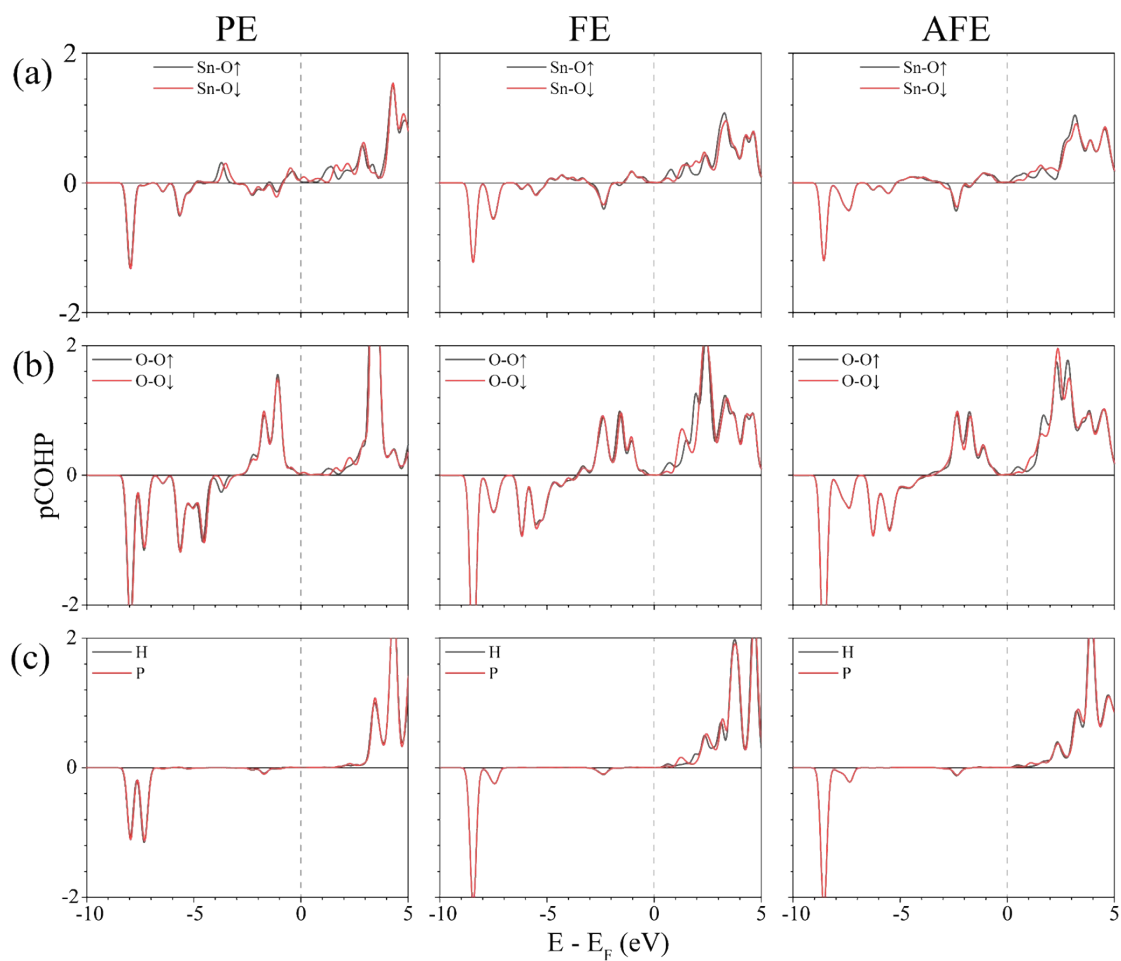

Figure S17. The COHP of (a) Sn-O, (b) O-O, and (c) O-H bonding in *OOH intermediate on PE-, FE-, and AFE-MnIrSn$_2$S$_6$ surface.
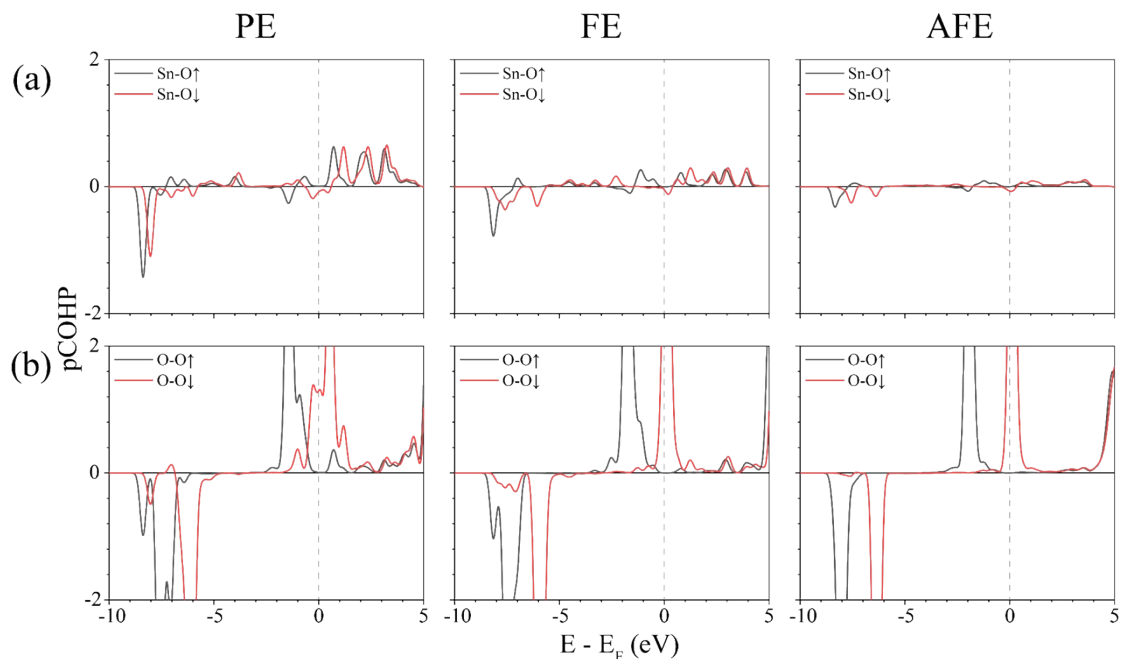
Figure S18. The COHP of (a) O-O and (b) O-H bonding in *OO intermediate on PE-, FE-, and AFE-MnIrSn$_2$S$_6$ surface.
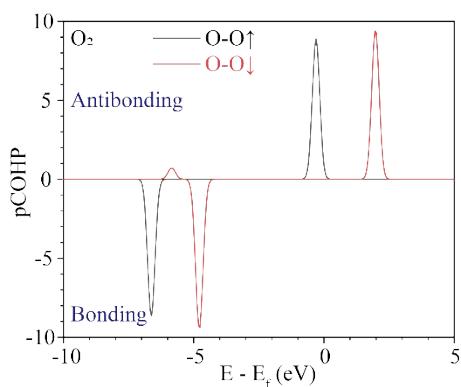

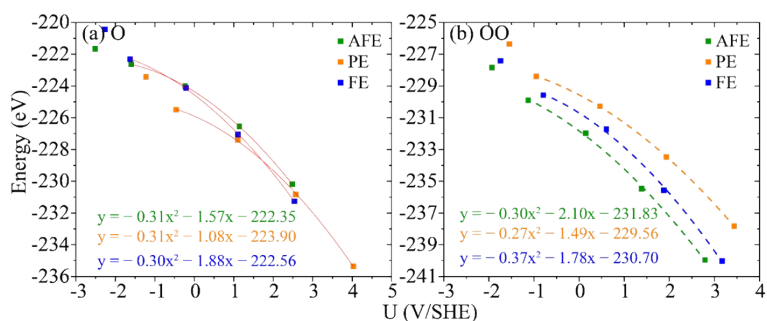
Figure S19. The COHP of O$_2$ molecule in vacuum.

Figure S20. The calculated potential vs. free energy relationship of (a) *O and (b) *OO intermediates on PE-, FE-, and AFE-MnIrSn$_2$S$_6$ surface. The fitting function is marked in the figure.
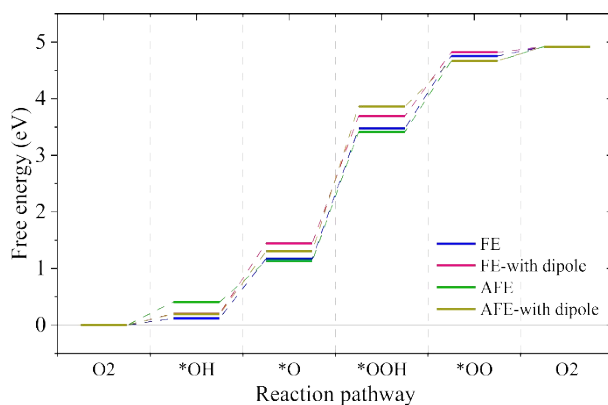
Figure S21. The stage plots with and without the dipole correction for AFE- and FE-MnIrSn$_2$S$_6$.

Reference

1. J. S. Filhol and M. Neurock, *Angew Chem Int Ed Engl*, 2006, **45**, 402-406.
2. C. D. Taylor, S. A. Wasileski, J.-S. Filhol and M. Neurock, *Physical Review B*, 2006, **73**.
3. Z. Duan and G. Henkelman, *ACS Catalysis*, 2020, **10**, 12148-12155.
4. A. Curutchet, P. Colinet, C. Michel, S. N. Steinmann and T. Le Bahers, *Phys. Chem. Chem. Phys.*, 2020, **22**, 7031-7038.
5. G. Buvat, M. J. Eslamibidgoli, S. Garbarino, M. Eikerling and D. Guay, *ACS Applied Energy Materials*, 2020, **3**, 5229-5237.
6. D. R. Kauffman, D. Alfonso, D. N. Tafen, J. Lekse, C. Wang, X. Deng, J. Lee, H. Jang, J.-S. Lee, S. Kumar and C. Matranga, *ACS Catalysis*, 2016, **6**, 1225-1234.
7. M. Li, L. Zhang, Q. Xu, J. Niu and Z. Xia, *J. Catal.*, 2014, **314**, 66-72.
8. R. Kishore, X. Cao, X. Zhang and A. Bieberle-Hütter, *Catal. Today*, 2019, **321-322**, 94-99.
9. X. Li, Z. Su, Z. Zhao, Q. Cai, Y. Li and J. Zhao, *Journal of Colloid and Interface Science*, 2022, **607**, 1005-1013.
10. S. Lin, X. Ye, X. Gao and J. Huang, *J. Mol. Catal. A: Chem.*, 2015, **406**, 137-144.
11. Z. Xue, X. Zhang, J. Qin and R. Liu, *Appl. Surf. Sci.*, 2020, **510**, 145489.
12. A. Chen, S. V. Nair, B. Miljkovic, H. E. Ruda and Z. Ji, *J. Electroanal. Chem.*, 2019, **855**, 113499.
13. F. Li, H. Ai, D. Liu, K. H. Lo and H. Pan, *Journal of Materials Chemistry A*, 2021, DOI: 10.1039/d1ta03412j.
14. H. Xiao, H. Shin and W. A. Goddard, *Proceedings of the National Academy of Sciences*, 2018, **115**, 5872-5877.
15. T. Wu, X. Ren, Y. Sun, S. Sun, G. Xian, G. G. Scherer, A. C. Fisher, D. Mandler,

J. W. Ager, A. Grimaud, J. Wang, C. Shen, H. Yang, J. Gracia, H.-J. Gao and Z. J. Xu, *Nature Communications*, 2021, **12**.

16. Z. Li, Z. Wang, S. Xi, X. Zhao, T. Sun, J. Li, W. Yu, H. Xu, T. S. Herng, X. Hai, P. Lyu, M. Zhao, S. J. Pennycook, J. Ding, H. Xiao and J. Lu, *ACS Nano*, 2021, **15**, 7105-7113.

17. H. Bai, S. Shen, F. Li, J. Geng, W. Feng, H. Liu, W. F. Ip, Y. Lu and H. Pan, *ChemSusChem*, 2022, DOI: 10.1002/cssc.202200280.